

Performance Analysis of Horizontal Axis Tidal Stream Turbine Considering the Effect of Blade Deformation

*Se Wan Park¹⁾, Sunho Park²⁾, and Shin Hyung Rhee³⁾

^{1), 2)} *Department of Naval Architecture & Ocean Engineering, Seoul National University,
Seoul, 151-744, Korea*

³⁾ *Department of Naval Architecture & Ocean Engineering, Research Institute of Marine
Systems Engineering, Seoul National University, Seoul, 151-744, Korea*

³⁾ shr@snu.ac.kr

ABSTRACT

In the present study, a numerical analysis method was developed to predict the performance of a 100-kW horizontal axis tidal stream turbine. Unsteady fluid flow around the turbine was studied using a RANS simulation technique based on a cell-centered finite volume method, and Shear Stress Transport $k-\omega$ model was used for the turbulence closure. The numerical analysis method was validated by comparing the results with the existing experimental data. The deformation of the blade caused by fluid pressure was simulated by the strongly coupled analysis method. The results drawn from the simulation without and with considering the deformation were compared in terms of power performance, cavitation inception, and vortex induced vibration at the blade tip.

1. INTRODUCTION

In recent years, interest in the renewable energy has risen since the environmental pollution and high oil price has been issues. Renewable energy, which comes from natural resources, can produce electricity with relatively less pollutions. Among the source of renewable energy, tidal stream energy has potential for a future electricity generation. Tides are more predictable than wind energy and solar power. Also, it has less pollution of visual and noise than others (MacLeod 2001).

There are many researches to analyze the performance of horizontal axis tidal stream turbines (HATST) numerically. Lee developed the element momentum theory (BEMT) code and applied to a HATST (Lee 2011). The results for the performance prediction of a turbine using BEMT showed similar to that using computational fluid dynamics (CFD) around the design tip speed ratio (TSR). Mason-Jones et al. (Mason-Jones 2008), and Kinnas and Xu (Kinnas 2009) analyzed three-dimensional turbines using CFD. Harrison et al. (Harrison 2009), and Lee et al. (Lee 2010) studied the wake effect on the turbine performance. Besides the general primitive variable-based formulation, McCombes et

¹⁾ Graduate Student

²⁾ Graduate Student

³⁾ Professor

al. (McCombes 2009) presented a numerical model based on the vorticity conserving form for unsteady wake modeling for marine current turbines.

Many researches on HATST were done with the assumption that the blade was sufficiently rigid body, which the effects of the blade deformation were negligible. However, a large chord to span ratio of HATST and high tidal current have a possibility to cause deformation of a turbine blade. Thus, computations of HATST have to include the fluid-structure interaction (FSI). However, many studies did not consider the interaction between fluid and structure for the design of HATST. Nicholls-Lee et al. optimized tidal energy extraction devices using the FSI analysis (Nicholls-Lee 2008). Nicholls-Lee et al. performed a FSI analysis by coupling BEM and FEM codes, and developed a FSI simulation procedure for the design of a 20m diameter and 3 bladed HATST (Nicholls-Lee 2011).

The present study focused on the numerical analysis of the tidal stream energy conversion turbine. The objectives are, therefore, (1) to predict performance of HATST by the computation without considering the deformation using finite volume method, and (2) to analyze it by the computation with considering the deformation. The results using the cases without and with the deformation were compared each other.

This paper is organized as follows. The description of the physical problem is presented first, and mathematical modeling method is followed. The computational method is introduced, and then the computational results are presented and discussed. Finally, concluding remarks are made.

2. NOMENCLATURE

C_P	Power coefficient [-]
C_{press}	Pressure coefficient [-]
R	Radius of turbine [m]
TSR	Tip speed ratio [-]
U_∞	Free stream velocity [m/s]
ρ	Density [kg/m ³]
Ω	Rotational speed [rad/s]

3. PROBLEM DESCRIPTION

A baseline turbine design was defined to show the feasibility of the developed procedures. A three-bladed HATST with a radius of 4 m was selected. The turbine blade was made of the NACA 63-418 foil section, which is popular blade section geometry for wind turbines. The foil shape was used beyond the hub to the blade tip, i.e., between $r/R = 0.2$ to 1.0. Unlike wind turbines, where a circular shape hub fitting is generally used, a 2:1 elliptic shape was adopted for the hub fitting. Generally, an elliptic hub is stronger than a circular one in flows with less frequent changes of direction such as the one in tidal stream.

The span-wise sections were designed to have various twist angles to extract a uniform lift force from each section. The chord lengths of each section ranged from 0.68 m at the root to 0.27 m at the blade tip.

The axis of the twist and center of each section were at 0.25C and 0.3C away from the leading edge, respectively. Here, C was the chord length. For the hub fitting part, there was no twist angle and the center was located at 0.5C.

The design revolution speed, Ω , was 24.72 rpm. The operating speed expressed by tip speed ratio (TSR) was defined as

$$TSR = \frac{R\Omega}{U_\infty} \quad (1)$$

where U_∞ is the free stream flow. TSR was set between 2.7 and 10.4, and the design TSR was 5.177. In the present study, TSR was varied by changing the free stream flow.

4. MATHEMATICAL MODELING

4.1. Finite Volume Method for Flow Analysis

The equations for the mass and momentum conservations were solved to obtain the velocity and pressure fields, respectively. Once the Reynolds averaging approach for turbulence modeling is applied, the equations for the mass and momentum conservation can be written as

$$\frac{\partial \rho}{\partial t} + \frac{\partial}{\partial x_j} (\rho U_j) = 0 \quad (2)$$

$$\frac{\partial \rho U_i}{\partial t} + \frac{\partial}{\partial x_j} (\rho U_i U_j) = -\frac{\partial p}{\partial x_i} + \frac{\partial}{\partial x_j} (\tau_{ij} - \overline{\rho u_i u_j}) + S_M \quad (3)$$

where U is the averaged velocity vector and p is the pressure. The unknown term, i.e., the Reynolds stress term, is related to the mean velocity gradients by the Boussinesq hypothesis, as follows:

$$-\overline{\rho u_i u_j} = \mu_t \left(\frac{\partial U_i}{\partial x_j} + \frac{\partial U_j}{\partial x_i} \right) - \frac{2}{3} \delta_{ij} \left(\rho k + \mu_t \frac{\partial U_k}{\partial x_k} \right) \quad (4)$$

where μ_t is the eddy viscosity or turbulent viscosity, which is modeled.

The SST k - ω turbulence model, which is based on the Boussinesq hypothesis with transport equations for the turbulent kinetic energy, k , and the turbulent frequency, ω , was adopted for turbulence modeling (Menter 1994). The turbulent viscosity is linked to the turbulence kinetic energy and turbulent frequency via the relation:

$$\mu_t = \rho \frac{k}{\omega} \quad (5)$$

And the turbulent kinetic energy and the turbulent frequency are obtained from the transport equations, respectively.

$$\frac{\partial(\rho k)}{\partial t} + \frac{\partial}{\partial x_j}(\rho U_j k) = \frac{\partial}{\partial x_j} \left[\left(\mu + \frac{\mu_t}{\sigma_k} \right) \frac{\partial k}{\partial x_j} \right] + P_k - \beta' \rho k \omega + P_{kb} \quad (6)$$

$$\frac{\partial(\rho \omega)}{\partial t} + \frac{\partial}{\partial x_j}(\rho U_j \omega) = \frac{\partial}{\partial x_j} \left[\left(\mu + \frac{\mu_t}{\sigma_\omega} \right) \frac{\partial \omega}{\partial x_j} \right] + a \frac{\omega}{k} P_k - \beta \rho \omega^2 + P_{\omega b} \quad (7)$$

where P_k is the production rate of turbulence, and here the model constants β' , a , β , σ_k , and σ_ω are 0.09, 5/9, 0.075, 2, and 2, respectively. The turbulent viscosity was used to calculate the Reynolds stresses to close the momentum equations. And the transport behavior can be obtained by a limiter to the formulation of the eddy-viscosity:

$$v_t = \frac{a_1 k}{\max(a_1 \omega, S F_2)} \quad (8)$$

where

$$v_t = \frac{\mu_t}{\rho} \quad (9)$$

F_2 is a blending function, which restricts the limiter to the wall boundary layer, as the underlying assumptions are not correct for free shear flows. S is an invariant measure of the strain rate.

4.1. Finite Element Method for Structural Analysis

FEM is a numerical technique which yields approximate solutions to differential equations that model problems arising in physics and engineering fields. The governing equations are integrated over each finite element and the solution summed over the entire problem. As a consequence of these operations, a set of finite linear equations is obtained in terms of a set of unknown parameters over each element. The solution of these equations is achieved using linear algebra techniques. The structure is assumed to be elastic and compressible. The governing equation is based on strains and constitutive equation as follows:

$$\int_{\Omega} \delta \varepsilon^T \sigma d\Omega - \int_{\Omega} \delta u^T b d\Omega - \int_{\Gamma} \delta u^T t d\Gamma = 0 \quad (10)$$

where to simplify the solution process, the boundary is split into Γ_u and Γ_t and the known traction boundary condition is introduced. It also imposes the displacement boundary conditions on the approximations for u and assumes that the virtual displacement δu vanishes on Γ_u . For linear elastic behavior the above equation simplifies to as follows

$$\int_{\Omega} \delta \varepsilon^T [\sigma_0 + D(\varepsilon - \varepsilon_0)] d\Omega - \int_{\Omega} \delta u^T b d\Omega - \int_{\Gamma_t} \delta u^T \bar{t} d\Gamma = 0 \quad (11)$$

In the finite element solution, we divide all integrals to be sums over individual elements and approximate the weak form by

$$\sum_e \int_{\Omega_e} \delta \varepsilon^T [\sigma_0 + D(\varepsilon - \varepsilon_0)] d\Omega - \sum_e \int_{\Omega_e} \delta u^T b d\Omega - \sum_e \int_{\Gamma_t^e} \delta u^T \bar{t} d\Gamma = 0 \quad (12)$$

where Ω_e and Γ_t^e denote element domains and the part of the boundaries of any element where tractions are specified, respectively. The approximation is associated with the fact that for curved boundary surfaces, the sum of the element domains, Ω_e , is not always exactly equal to Ω , nor is the sum of Γ_t^e equal to Γ_t . This is easily observed for approximations using linear elements (Zienkiewics 2005).

5. COMPUTATIONAL METHODS

5.1. Numerical Methods

A pressure-based finite volume method was employed. Time derivative terms were discretized using the second-order accurate backward implicit scheme, which was generally recommended for most transient computations (ANSYS Inc 2010). The advection terms were discretized using a high resolution scheme, which had second-order accuracy. The velocity-pressure coupling was based on the discretization scheme, proposed by Rhie and Chow [Rhie 1982]. The commercial CFD code, ANSYS CFX 13.0 was used for solving fluid domain. ANSYS Transient Structural was employed for solving the transient structural problem.

5.2. Solution Domain, Boundary Conditions, and Mesh

The Cartesian coordinate system adopted was such that the positive x-axis was in the stream-wise direction, the positive y-axis toward the right-hand side direction, and the positive z-axis was in the vertically upwind direction. The origin of the coordinate system was located at the hub center. Thus the x-axis was the rotational axis with a rotor revolving in the counter clockwise direction.

A rotating reference frame was used to accommodate the rotation of the rotor in open water conditions. It is one of the simplest approaches for a modeling problem that involves rotating zones. With the rotating reference frame, only one blade needed to be modeled with periodic boundaries on the sides. The computational domain extent was a length of $9D$ and a radius of $3D$, where D represented the turbine diameter. The inlet and outlet boundaries were located at $3D$ upstream and $6D$ downstream, respectively.

Fig. 1 shows the boundary condition and domain extents designed for the present computation. The Dirichlet boundary condition, i.e., the specified value of the velocity, was applied on the inlet boundary. On the exit boundary, the reference pressure with extrapolated velocity was applied. The free slip wall boundary condition was applied on the far-field boundary. A no-slip condition and FSI interface condition was applied on the turbine blade surfaces. Non-matching interfaces, between the sub-domain near the turbine blade and outer sub-domains, were defined and solved using general grid

interface (GGI) interpolation method. On the side boundary, to take the rotational flow into account, the flow across the two opposite planes was assumed to be identical, i.e., periodic.

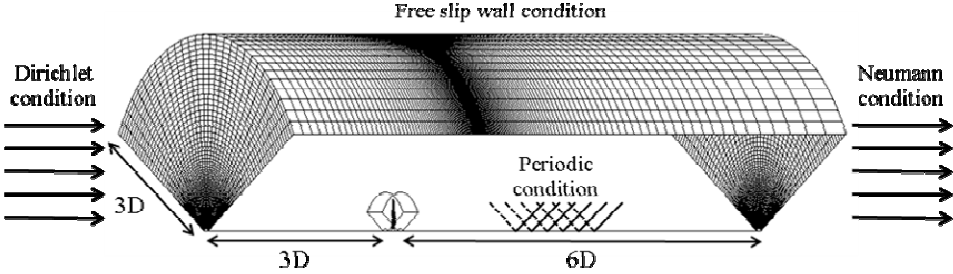


Fig. 1 Computational domain for the CFD analysis

To develop a convenient procedure for performance prediction, hybrid meshing was used (Lee 2011). The whole domain was divided into several sub-domains, and among the sub-domains, the one with the blade was filled with tetrahedral cells and the others with simple geometry were filled with hexahedral cells for high quality solution, as shown in Fig. 2. By this approach, it was possible to get rid of the difficulty of mesh generation around complex geometry.

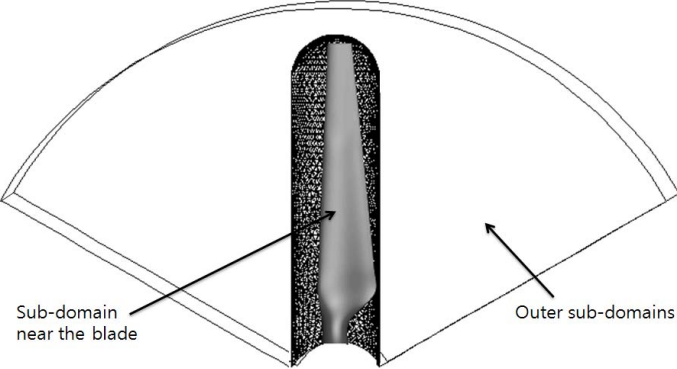


Fig. 2 Sub-domain near the blade for the CFD analysis

On the rotating turbine blade, a high speed flow occurs near the blade tip and low pressure appears near the leading edge and at the blade tip on the suction side. Accurate prediction of the low pressure on the suction side is necessary for the high fidelity performance prediction of turbines. Thus, the blade surface near the leading edge, trailing edge, and blade tip were filled with finer cells. An unstructured mesh consisting of 2 million cells in the domain were generated and employed for the computations.

Fig. 3 shows the surface mesh for the finite element analysis. For more accurate prediction of deformation, fine meshes were distributed in the leading edge of the blade.

The structured surface mesh was consisted of 70 meshes in the chord-wise and 15 meshes in the span-wise directions. The turbine blade is constructed of the E-glass reinforcing fiber, and its material property is shown in Table 1 (Shenoi 1993).

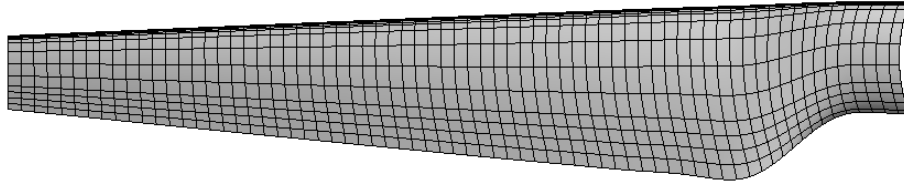


Fig. 3 Surface meshes for the structural analysis

Table 1 Mechanical properties of the E-glass reinforcing fiber (Shenoi 1993)

Property	Value
Density (kg/m^3)	2550
Young's Modulus (GPa)	72
Poisson's Ratio	0.2

5.2. Verification Test

To verify the developed CFD procedure, the results from the model scale experiment reported by Bahaj et al. were used (Bahaj 2007). A three-bladed 800 mm diameter turbine was used. The blade geometry was defined with 17 sections in the span-wise direction. Each blade section took the profile shape of a NACA 63-8xx. The chord, thickness, and pitch distribution were also provided. A commercial CAD tool, CATIA, was used to construct the blade geometry with the given information. Fig. 4 shows the test rig in the cavitation tunnel and the CAD constructed blade geometry.

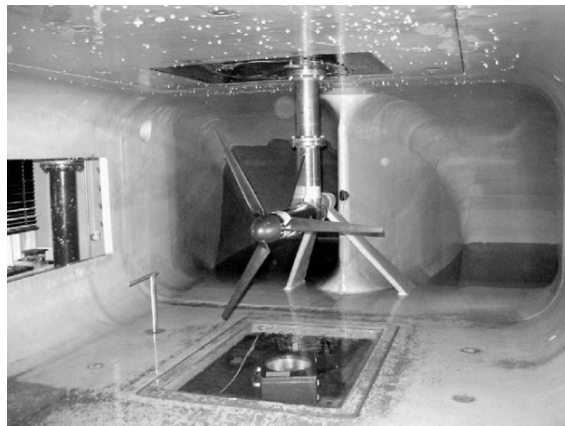


Fig. 4 Photograph of the test rig in the cavitation tunnel (Bahaj et al., 2007)

The experiments were done in a 2.4 m × 1.2 m cavitation tunnel. The results for the power coefficient were presented for a wide range of *TSR*. The turbine performance was analyzed for a 0° yaw angle and 25° hub pitch angle conditions. The turbine dimensions and inflow velocity of 1.54 m/s were the same for both the measurements

and CFD predictions. Note that the hub, however, was not considered in the CFD prediction. And only one blade was used for the prediction since a rotating reference frame method was employed. Fig. 5 shows the power coefficient ($C_P = P/0.5\rho AU_\infty^3$) over a range of TSR published by the experiment and predicted by the present CFD method. The present CFD results agree well with the experimental data.

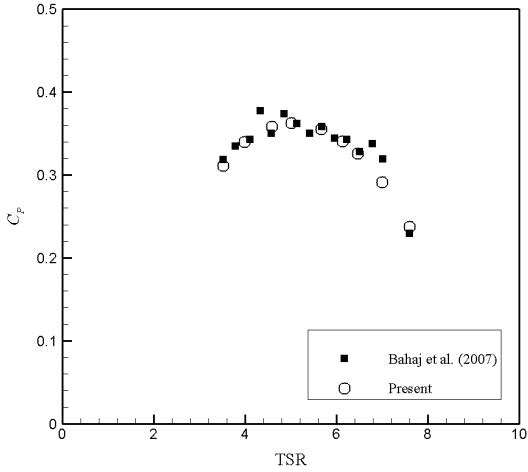


Fig. 5 Verification for the C_P

5. RESULTS AND DISCUSSION

Before the FSI analysis, the computation of the flow around the baseline turbine without considering the deformation was performed using the verified computational methods. Fig. 6 shows the predicted C_P over a range of various $TSRs$, presenting a typical trend of the power performance curve for a three-bladed tidal turbine. The peak power coefficient was predicted at the design TSR , 5.177.

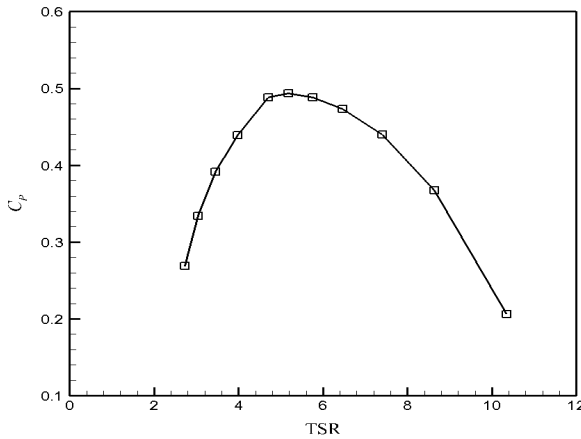


Fig. 6 C_P curve of the baseline turbine

The surface pressure coefficient ($C_{press} = (P_L - P_O)/0.5\rho U_\infty^2$) contours on the pressure and suction sides of the baseline turbine at the design TSR are shown in Fig. 7. The lowest pressure was seen at the leading edge on the suction side near the blade tip. Meanwhile, the highest pressure was observed at the leading edge on the pressure

side. The pressure difference between the two sides generates the lift force on the blade, and thereby the torque on the turbine. From the pressure coefficient contours, it was obvious that most of the power was produced near the blade tip.

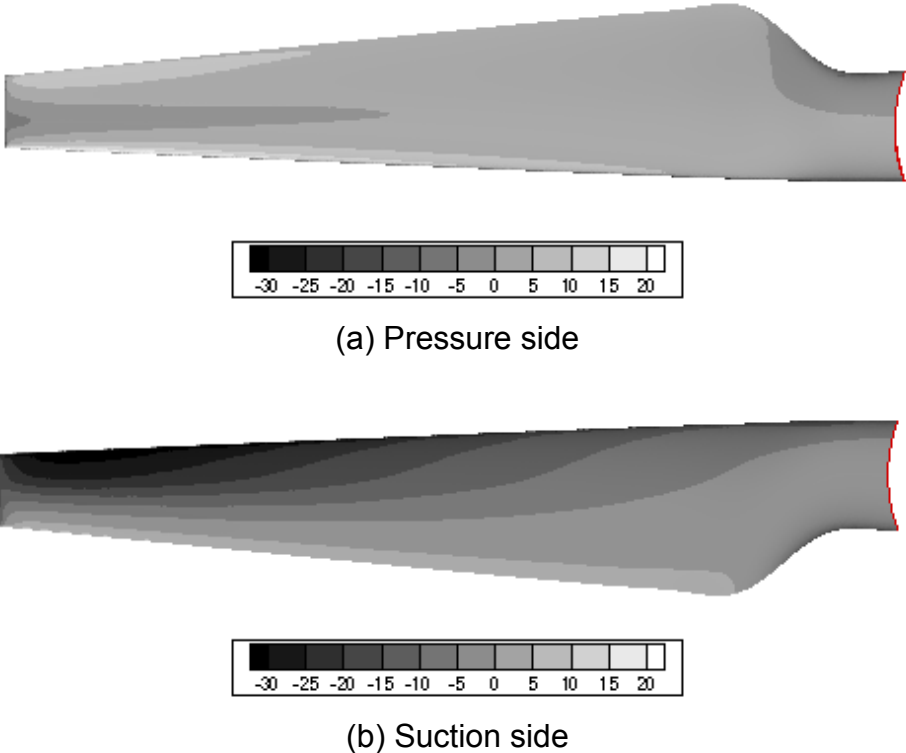


Fig. 7 Surface C_{press} contours on the pressure and suction sides by the simulation w/o considering the blade deformation

The FSI analysis was carried out at design TSR . The tidal current caused deformation of the blade and then deformation of the blade stopped at the equilibrium level, which the fluid force and structure restoring force were balanced. Fig. 8 shows the tip displacement of the baseline turbine blade. The predicted equivalent displacement at the tip of the blade was $0.022\ m$. Fig. 9 shows the deformed shape of the blade, which is exaggerated by 20 times. The turbine blade was bent toward the downstream. Fig. 10 shows the von Mises stress distribution on the pressure and suction sides of the blade. The maximum stress was observed at the mid-chord for the range of $r/R=0.4\sim 0.5$.

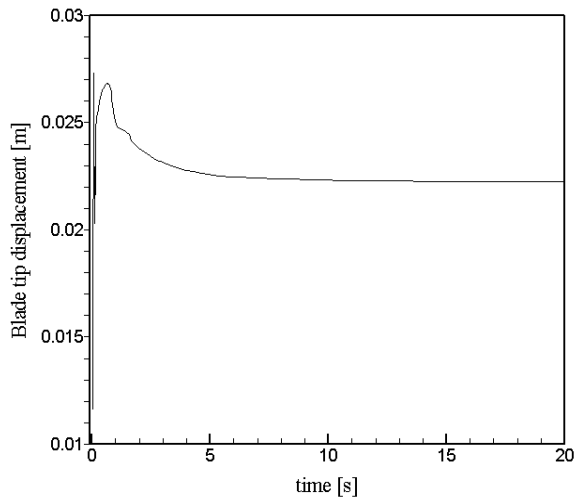
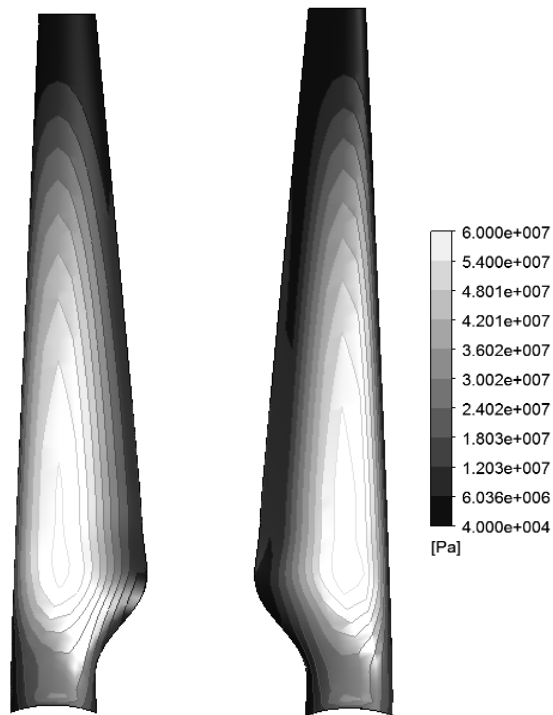


Fig. 8 Blade tip displacement



Fig. 9 Deformed blade shape exaggerated by 20 times



(a) Pressure side (b) Suction side
Fig. 10 von Mises Stress distribution

Fig. 11 shows the surface pressure coefficient contours on the pressure and suction sides of the baseline turbine at the design *TSR*. The lowest pressure was also seen at the leading edge on the suction side near the blade tip. The pressure coefficient on the suction side computed by the case of the deformation considered was overall lower, compared to the case without considering the deformation. Table 2 lists the minimum

and maximum pressure coefficient levels on the blade surface. The maximum pressure coefficient level was same for two cases, while the minimum pressure coefficient was lower when the deformation was not considered. Deformation of the blade reduced the pressure drop at the suction side. In terms of the minimum pressure on the suction side, the computation without considering the deformation could over-predict the cavitation.

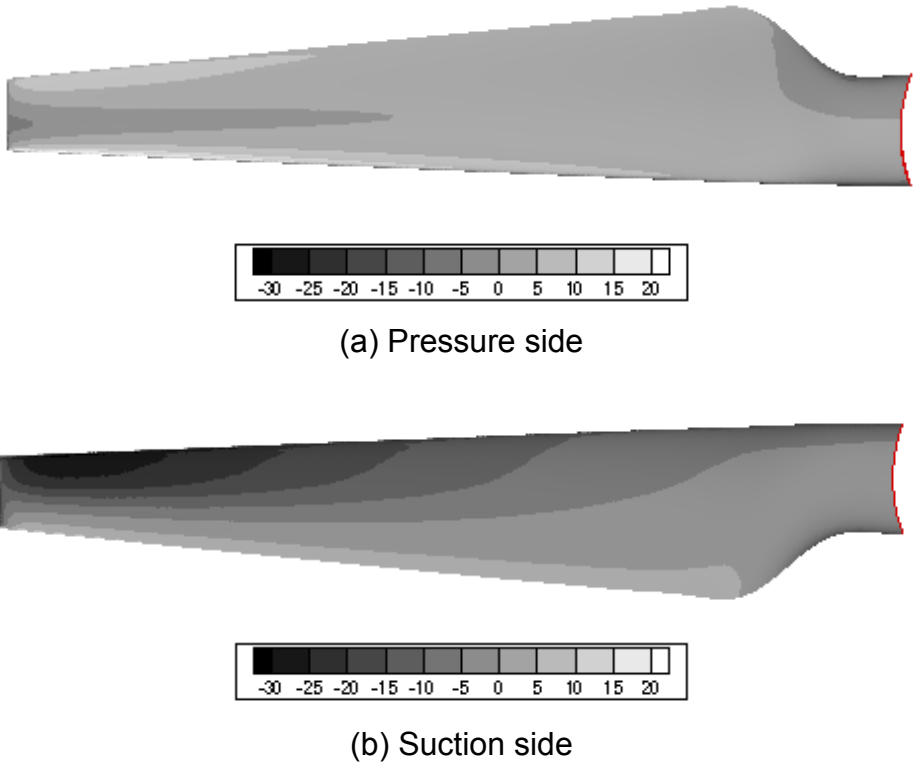


Fig. 11 Surface C_{press} contours on the pressure and suction side by the simulation w/ considering the deformation

Table 2 Minimum and maximum C_{press} levels		
	w/o the deformation	w/ the deformation
Minimum C_{press}	-36.5	-31.3
Maximum C_{press}	22.4	22.4

Fig. 12 shows the power coefficient predicted for the cases without and with the deformation. In the case of the deformation considered, the power coefficient was 2.7% lower at the design TSR . Namely, the computation without considering the deformation could over-predict the turbine performance. It confirms that the FSI analysis is essential to predict the performance of a HATST exactly.

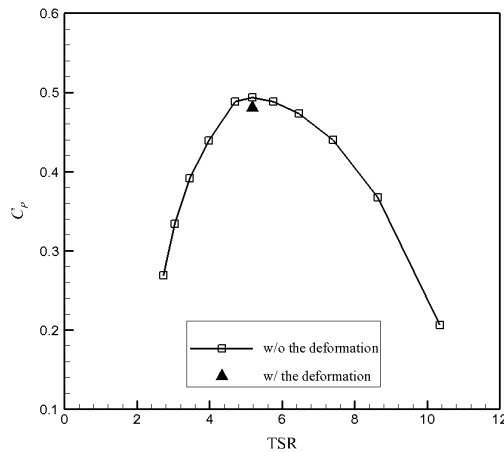


Fig. 12 Comparison of the C_p by the simulations w/o and w/ the deformation

The pressure coefficient contours and streamlines for span-wise sections at $r/R = 0.7$ and 0.9 are shown in Fig. 13. The plotted area was $-0.3 \leq x \leq 0.3$ and $-0.3 \leq y \leq 0.3$. The flow patterns for the pressure coefficient distribution for two cases were very similar. At the case of the deformation considered, the minimum pressure was increased on the suction side, compared to the case without considering the deformation. Fig. 14 shows the vorticity magnitude contours at the downstream of the blade. Also, the maximum vorticity level was decreased by considering the deformation

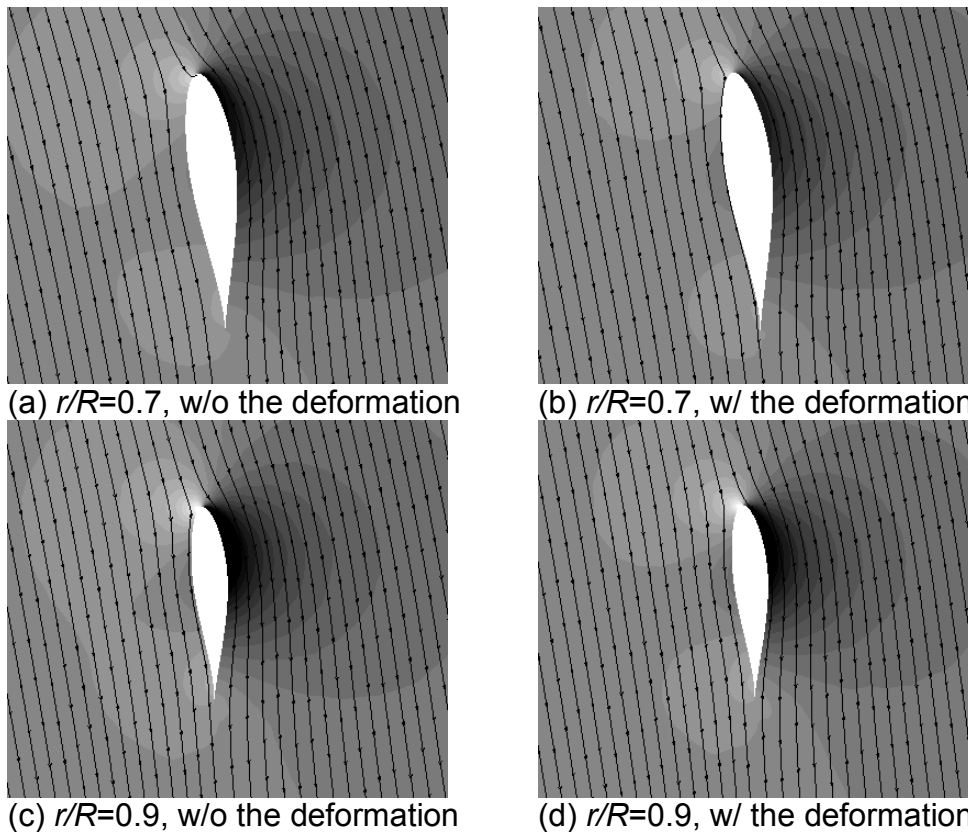


Fig. 13 $C_{p_{press}}$ Contours and streamlines of the cross-section

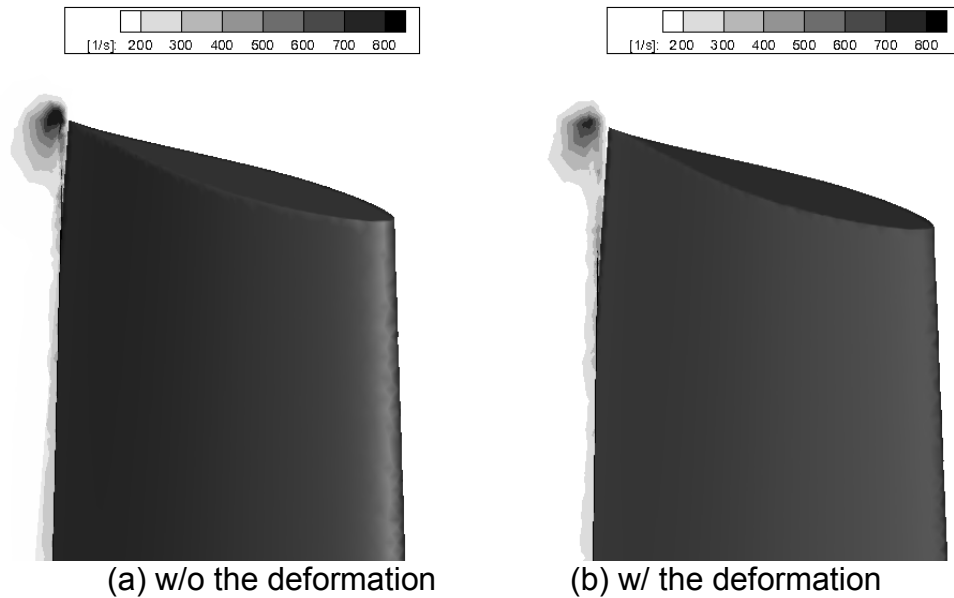


Fig. 14 Vorticity magnitude contours

CONCLUSION

The FSI analysis was performed for the HATST. Both the fluid and structure analysis methods were coupled together to analyze the FSI.

The computational methods were verified by comparing against existing experimental data. The power coefficients over a range of *TSR* were showing good agreement.

The CFD analysis without considering the deformation was done between 2.7 and 10.4 *TSR*. And the FSI analysis was performed at the design *TSR*. In the FSI analysis, feasible deformation of the blade tip and von Mises stress were computed. The FSI analysis was essentially needed to predict performance of the HATST with accuracy, since the difference of the predicted performance between the cases without and with the deformation was remarkable. In conclusion, the FSI analysis should be considered for better turbine blade design.

ACKNOWLEDGMENTS

This work was supported by the Ministry of Knowledge Economy (20093021070010, 20104010100490), and the the Ministry of Education, Science and Technology (R32-2008-000-10161-0).

REFERENCES

- ANSYS Inc. (2010), ANSYS CFX 13.0 Modeling Guide.
 Bahaj, A.S., Molland, A.F., Chaplin, J.R., Batten W.M.J. (2007), "Power and thrust measurements of marine current turbines under various hydrodynamic flow conditions in a cavitation tunnel and a towing tank", *Renewable Energy*, 32, 407-426.

Harrison, M.E., Batten, W.M.J., Myers, L.E., Bahaj, A.S. (2009), "A comparison between CFD simulations and experiments for predicting the far wake of horizontal axis tidal turbines", 8th European Wave and Tidal Energy Conference, Uppsala.

Kinnas, S.A., Xu, W. (2009), "Analysis of tidal turbines with various numerical methods", 1st Annual MREC Technical Conference, MA.

Lee, J. H., Kim, D. H., Rhee, S. H. (2011), "Horizontal axis tidal stream turbine analysis using numerical simulation", 49th AIAA, Orlando.

Lee, S.H., Lee, S.H., Jang, K., Lee, J., Hur, N. (2010), "A numerical study for the optimal arrangement of ocean current turbine generators in the ocean current power parks". *Current Applied Physics* 10, 137–141.

McCombes, T., Johnstone, C., Grant, A. (2009), "Unsteady 3D wake modeling for marine current turbines", 8th European Wave and Tidal Energy Conference, Uppsala.

MacLeod, A.J., Barnes, S., Rados, K.G., Bryden, I.G. (2001), "Wake effects in tidal current turbine farms", Marine Renewable Energy Conference, Newcastle.

Mason-Jones, A., O'Doherty, T., O'Doherty, D.M., Evans, P.S., Wooldridge, C.F. (2008), "Characterisation of a HATT using CFD and ADCP site data", 10th World Renewable Energy Congress, Glasgow.

Menter, F.R. (1994), "Two-equation eddy-viscosity turbulence models for engineering applications", *AIAA-Journal.*, 32(8), 1598-1605.

Nicholls-Lee, R.F., Turnock, S.R., and Boyd, S.W. (2008), "Simulation based optimization of marine current turbine blades", 7th International Conference on Computer and IT Applications in the Maritime Industries, Liege.

Nicholls-Lee, R.F., Turnock, S.R., and Boyd, S.W. (2011), "A method for analysing fluid structure interactions on a horizontal axis tidal turbine", 9th European Wave and Tidal Energy Conference, Southampton.

Rhie, C.M., and Chow, W.L. (1982), "A numerical study of the turbulent flow past an isolated airfoil with trailing edge separation", AIAA Paper 82-0998.

Shenoi R. A. and Wellicome J.F. (1993), *Composite Materials in Maritime Structures*, CAMBRIDGE UNIVERSITY PRESS, UK

Wood, C., Gill, A.J., Hassan, O., and Bonet, J. (2008), "A partitioned coupling approach for dynamics fluid-structure interaction with applications to biological membranes", *Int. J. Numer. Meth. Fluids* 57, 555-581.

Zienkiewics, O.C., and Taylor, R.L. (2005), *The finite element method*, Oxford, UK.